Supporting Information

Synergistic Integration of Disordered Tm:$CaGdAlO_4$ Single-Crystal Fibers with Oxidation-Resistant MXene for High-Performance 2 μm Lasers

Xiaofei Ma,[†ab]* Mingji Zhang,[†c] Tao Wang,[c] Xuesong Li,[d] Xiangfei Zhu,[ab] Zefeng Wang,[ab] Jian Zhang,*[c] Zhitai Jia[c] and Xutang Tao[c]

[a]*College of Advanced Interdisciplinary Studies, National University of Defense Technology, Changsha, China.*

[b]*Nanhu Laser Laboratory, National University of Defense Technology, Changsha, China. Email: xiaofeima_@nudt.edu.cn*

[c]*State Key Laboratory of Crystal Materials and Institute of Crystal Materials, Shandong University, Jinan 250100, China. Email: jian.zhang@sdu.edu.cn*

[d]*School of Nuclear Science and Engineering, North China Electric Power University, Beijing 102206, China.*

† These authors contributed equally to this work.

*Corresponding author

Email: xiaofeima_@nudt.edu.cn, jian.zhang@sdu.edu.cn

S1. Material Characterization of Oxidation-Resistant MXene (OR-$Ti_3C_2T_x$)

To confirm the phase purity, layered structure, and oxidation-resistant nature of the OR-$Ti_3C_2T_x$ saturable absorber used in this work, comprehensive material characterizations were performed. The same batch of OR-$Ti_3C_2T_x$ dispersion was used for all optical measurements and device integration, ensuring consistency between the Z-scan experiments and the laser cavity device.

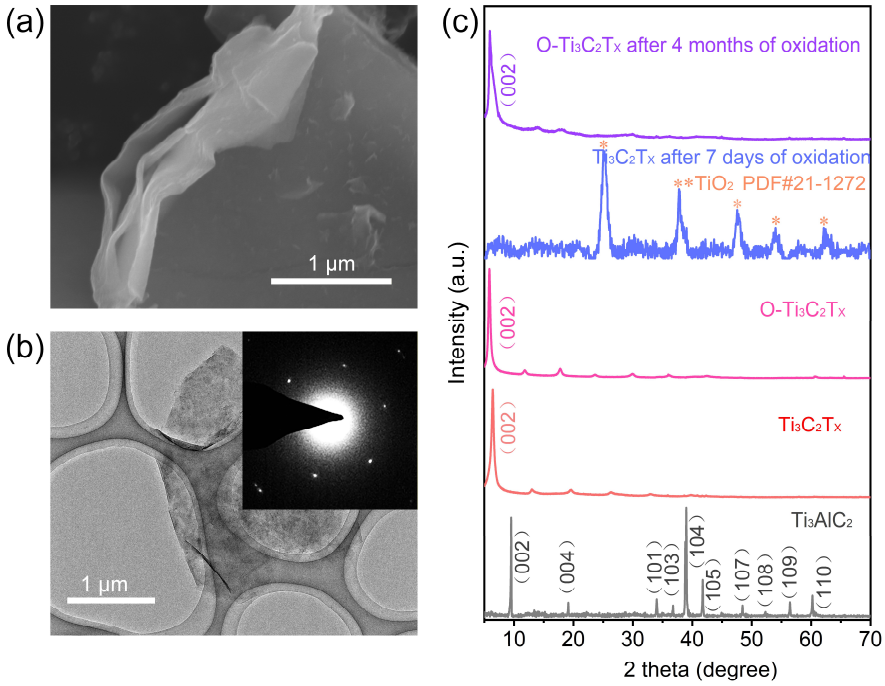

Figure S1. Characterization of the oxidation-resistant OR-$Ti_3C_2T_x$ MXene saturable absorber (SA). (a) Scanning electron microscopy (SEM) images of the layered OR-$Ti_3C_2T_x$. (b) Transmission electron microscopy (TEM) image of a single-layer OR-$Ti_3C_2T_x$ nanosheet. Inset: The selected-area electron diffraction (SAED) pattern. (c) X-ray diffraction (XRD) patterns of the precursor Ti_3AlC_2, conventional $Ti_3C_2T_x$, the as-synthesized OR-$Ti_3C_2T_x$ from this work, and OR-$Ti_3C_2T_x$ aged in ambient air for 4 months.

Scanning electron microscopy (SEM) images reveal that OR-$Ti_3C_2T_x$ possesses a well-defined layered microstructure with substantial lateral dimensions and apparent flexibility (**Figures S1a**). Transmission electron microscopy (TEM) further confirms the existence of large, single-layer sheets (**Figure S1b**). The corresponding selected-

area electron diffraction (SAED) pattern (inset of **Figure S1b**) exhibits a regular hexagonal arrangement of diffraction spots, verifying the high crystalline quality and hexagonal symmetry of the synthesized material.

X-ray diffraction (XRD) analysis provides insight into the material's structural evolution and stability (**Figure S1c**). The pattern of the precursor Ti_3AlC_2 (black line) shows no impurity phases. The XRD profile of the as-prepared OR-$Ti_3C_2T_x$ (pink line) is largely consistent with that of conventional $Ti_3C_2T_x$ (red line), with only a minor downshift in the (002) peak, indicating that the surface treatment preserves the core crystal lattice. Crucially, aging tests demonstrate the superior environmental stability of the optimized material. While conventional $Ti_3C_2T_x$ displays characteristic TiO_2 peaks after only 7 days in ambient air (blue line), the OR-$Ti_3C_2T_x$ sample shows no signs of TiO_2 formation even after 4 months (purple line), underscoring its enhanced oxidation resistance.

S2. Z-scan Data Processing

The saturable absorption characteristics and parameters of the stable MXene and BiOCl SA can be measured by open-aperture (OA) Z-scan experiments. In the theoretical model of nonlinear optics, when the laser passes through the sample along the Z direction, it can be expressed by the following equation:

$$\frac{dI}{dZ} = -\alpha(I)I \qquad \text{S(1)}$$

where, I is the incident light intensity, Z is the position of the sample, α (I) is the absorption coefficient of the sample, which can be expressed as:[1]

$$\alpha(I) = \alpha_0 + \beta I \qquad \text{S(2)}$$

α_0 and β respectively represent the linear and nonlinear absorption coefficient of the sample. The linear absorption coefficient can be directly measured, and the nonlinear absorption part can be obtained by fitting the aperture Z scan data:[2]

$$T_n = \sum_{n=0}^{\infty} \frac{(-\beta I_0 L_{eff})^n}{\left(1+\frac{Z^2}{Z_0^2}\right)^n (n+1)^{\frac{3}{2}}} \approx 1 - \frac{\beta I_0 L_{eff}}{2^{\frac{3}{2}}\left(1+\frac{Z^2}{Z_0^2}\right)} \qquad \text{S(3)}$$

$$L_{eff} = \frac{1-e^{-\alpha_0 L}}{\alpha_0} \qquad \text{S(4)}$$

where Z is the sample position, T_n is the nonlinear transmittance; I_0 is the peak power density at the focal point (Z=0), Z_0 is the Rayleigh length of the detection light, L_{eff} is the effective length; α_0 Is the linear absorption coefficient, L is the sample thickness, and β is the nonlinear absorption coefficient. For saturated absorption, β is a negative value, while for anti-saturated absorption, β is a positive value. Since β is related to the imaginary part $Im(\chi^{(3)})$ of the third-order nonlinear polarizability, it can be obtained as:[3]

$$Im(\chi^{(3)}) = (1.04 \times 10^{-9} \frac{c\lambda n^2}{\pi})\beta \quad \text{S(5)}$$

where, c is the speed of light, λ is the wavelength of the incident laser, n is the refractive index of the sample.

When both saturated absorption and anti-saturated absorption exist, the Equation S2 can also be expressed as:[4]

$$\alpha(I) = \frac{\alpha_0}{1+\frac{I}{I_S}} + \beta_{eff} I \quad \text{S(6)}$$

Among them, the first term of the above formula describes the saturated absorption behavior, I_s is the saturation intensity of the sample; the second term describes the anti-saturated absorption behavior (such as two-photon absorption), and β_{eff} is the two-photon absorption coefficient of the sample. When β_{eff} =0, it means that there is only saturated absorption behavior in the sample. Combining Equation S1 and S6, we can get:

$$\frac{dI}{dZ} = -(\frac{\alpha_0}{1+\frac{I}{I_S}} + \beta_{eff} I)I \quad \text{S(7)}$$

Further transformation can obtain the fitting equation:

$$T_n = (1 - \frac{\Delta R I_S}{I_S + \left(\frac{I_0}{1+\frac{Z^2}{Z_0^2}}\right)} - \frac{\beta_{eff} L_{eff} I_0}{1+\frac{Z^2}{Z_0^2}})/(1 - \Delta R) \quad \text{S(8)}$$

The variation in transmittance with incident intensity is shown in the Figure S1. The following saturated absorption equation[5] can be used to fit the data:

$$T = Aexp(\frac{-\Delta R}{1+\frac{I}{I_S}}) \quad \text{S(9)}$$

where I is the incident light intensity, A is a normalized parameter, T is the transmittance.

Fitting the Z-scan curve by the above formula, the modulation depth ΔR, saturation intensity I_s, nonlinear absorption coefficient β and two-photon absorption coefficient β_{eff} of the sample can be obtained.

S3. Continuous Wave and Pulse Laser Data

Table S1. Summary of Tm: $CaGdAlO_4$ (Tm: CGA) SCF Continuous wave laser results

Laser cavity type	Input mirror / L2 length [mm]	T_{OC} [%]	Output laser power [W]	Slope efficiency [%]	λc [nm]
V-cavity	10	2	1.262	16.004	1959.140
	15	2	1.278	16.136	1955.914
	20	2	1.437	19.096	1981.720
	25	2	1.450	18.668	1953.763
V-cavity	10	5	1.352	14.930	1993.550
	15	5	1.482	16.429	1981.720
	20	5	1.573	18.963	1992.470
	25	5	1.611	19.202	1975.270
straight cavity	-	2	2.702	22.426	1990.320
	-	5	3.338	27.307	1982.800

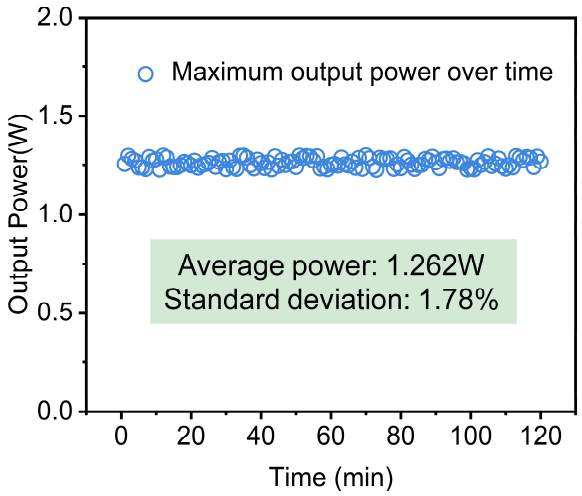

Figure S2. Stablity of laser the power fluctuation profile of the passively Q-switched Tm:CGA SCF laser under the maximum output power over a 2-hour continuous operation period

Table S2. Passively Q-switched laser performance of the Tm:CGA SCF integrated with the OR-$Ti_3C_2T_x$ SA.

OC	Pulse duration [ns]	Repetition rate [kHz]	Output power [W]	Single pulse energy [μJ]	Peak power [W]	λc [nm]
T=2%	580	81.00	0.676	8.350	14.39	1984.95
T=5%	490	80.16	1.262	15.74	32.13	1978.50

S4. Ray-tracing Analysis of Pump Propagation in the SCF

To understand and optimize the pump light delivery within the Tm:CGA single-crystal fiber (SCF), ray-tracing simulations based on geometrical optics were performed. Figure S3a illustrates the simulated longitudinal and transverse intensity distributions of the pump beam at various axial positions. The pump light is initially focused onto the input facet of the SCF. It then diverges within the crystal until encountering the core-air interface, where total internal reflection (TIR) occurs. This TIR confinement guides the pump radiation along the fiber, leading to a progressive homogenization of the transverse intensity profile. The evolution from a focused spot to a ring-shaped distribution (at z = 6 mm) and finally to a quasi-flat-top beam (with a diameter of ~350 μm) is clearly visualized, indicating efficient spatial overlap preparation for the gain medium.

The waveguiding effectiveness is further quantified in Figure S3b, which plots the on-axis normalized intensity (I/I_max) along the propagation direction. Due to the confinement effect, the intensity remains remarkably high over considerable lengths, retaining 57% of its peak value at z = 9.5 mm and approximately 50% at z = 18 mm. This performance is in stark contrast to free-space propagation, where diffraction would cause a rapid intensity decay. This analysis confirms the SCF's capability for efficient pump guidance, which is critical for achieving high gain and effective power scaling.

Therefore, the 8 mm SCF length used in our experiments represents an optimized

design that ensures strong pump guidance, efficient gain extraction, and manageable thermal load, all critical for high-power continuous-wave and pulsed laser operation.

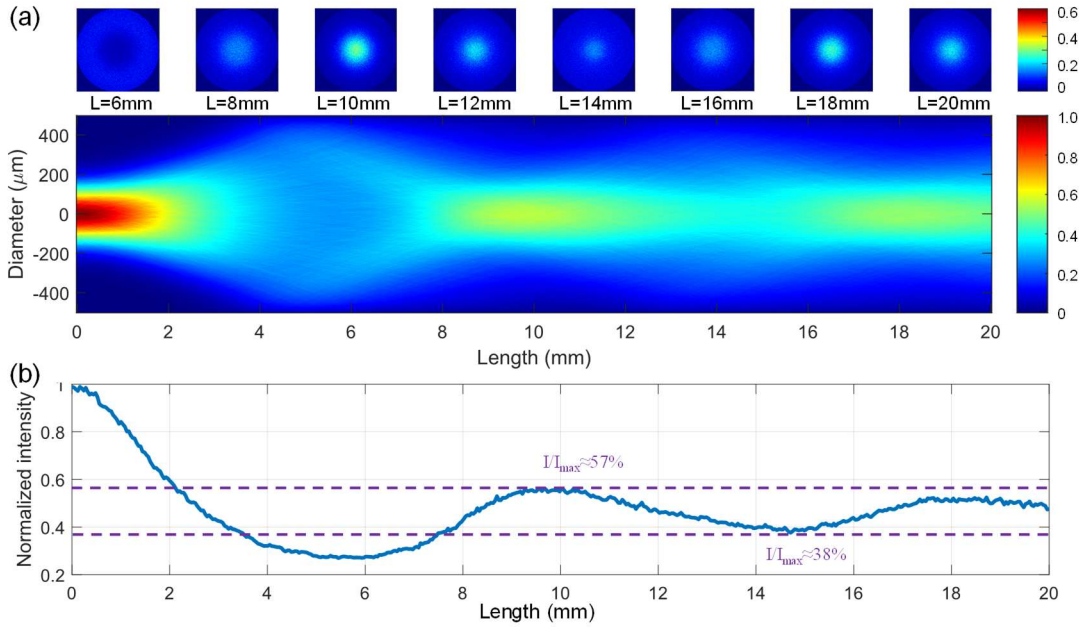

Figure S3. Ray-tracing analysis of pump light propagation in the Tm:CGA single-crystal fiber. (a) Simulated evolution of the longitudinal and transverse intensity distributions of the pump laser within the SCF. (b) Variation of the normalized on-axis intensity along the propagation distance in the SCF under the waveguiding effect.

S5. Passively Q-Switched Pulsed Lasers Realized by Combining Tm^{3+}-Doped Gain Media with Different Saturable Absorbers

Table S3. Results of Passively Q-Switched Pulsed Lasers Realized by Combining Tm^{3+}-Doped Gain Media with Different Saturable Absorbers

SA	Gain Medium	λ(nm)	Mean Power (W)	Single Pulse Energy (μJ)	Pulse Duration (ns)	Repetition Rate (kHz)	Ref.
MoS_2	Tm:$CaYAlO_4$	1850	0.490	4.87	480	102.6	[6]
MoS_2	Tm:YAG	2330	0.204	1.07	150	190	[7]
Graphdiyne	Tm:YAG	2007.6	1.044		895	180.5	[8]
MoS_2	Tm:CLNGG	1977	0.062	0.72		110	[9]
Cr^{2+}:ZnS	Tm,Ho:LLF	2055	0.074	13	12000	5.8	[10]
OR-MXene	Tm:CGA SCF	1979	1.262	15.74	490	80.16	This Work

References

[1] K. Wang, B.M. Szydłowska, G. Wang, X. Zhang, J.J. Wang, J.J. Magan, L. Zhang, J.N. Coleman, J. Wang, W.J. Blau, *ACS Nano* **2016**, 10, 6923.

[2] J. Guo, D. Huang, Y. Zhang, H. Yao, Y. Wang, F. Zhang, R. Wang, Y. Ge, Y. Song, Z. Guo, F. Yang, J. Liu, C. Xing, T. Zhai, D. Fan, H. Zhang, *Laser Photonics Rev.* **2019**, 13, 1900123.

[3] Y. Feng, N. Dong, G. Wang, Y. Li, S. Zhang, K. Wang, L. Zhang, W.J. Blau, J. Wang, *Opt. Express* **2015**, 23, 559.

[4] H. Yang, X. Feng, Q. Wang, H. Huang, W. Chen, A.T.S. Wee, W. Ji, *Nano Lett.* **2011**, 11, 2622.

[5] E. Garmire, *IEEE J. Sel. Top. Quantum Electron.* **2000**, 6, 1094.

[6] J. Lan, X. Zhang, Z. Zhou, B. Xu, H. Xu, Z. Cai, N. Chen, J. Wang, X. Xu, R. Soulard and R. Moncorgé, *IEEE Photonics Technol. Lett.* **2017**, 29, 515.

[7] F. Zha, X. Yu, H. Chu, H. Pan, S. Zhao, P. Loiko, Z. Pan and D. Li, *Opt. Lett.* **2022**, 47, 6265.

[8] Q. Wu, Y. Wang, G. Zhao, Y. Hu, M. Wang and W. Huang, *Infrared Phys. Technol.* **2023**, 134, 104914.

[9] L. C. Kong, G. Q. Xie, P. Yuan, L. J. Qian, S. X. Wang, H. H. Yu and H. J. Zhang, *Photon. Res.* **2015**, 3, A47.

[10] X. Zhang, L. Yu, S. Zhang, L. Li, J. Zhao and J. Cui, *Opt. Express* **2013**, 21, 12629.